Journal of Materials Chemistry A

ROYAL SOCIETY OF CHEMISTRY

PAPER

View Article Online
View Journal | View Issue

Cite this: J. Mater. Chem. A, 2025, 13, 28160

Rational design of metal node-modified Ti-based MOFs for selective photoreduction of carbon dioxide to ethanol by computational screening†

Shuang Wang,‡[a] Xiaowa Nie, ‡*[a] Chunshan Song *[b] and Xinwen Guo *[a]

In this work, density functional theory (DFT) calculations were conducted to investigate a series of metal node-modified Ti-MOF catalysts using transition metals (Mn, Fe, Co, Ni, Cu, Zn, Zr, Nb, Mo, Ru, Rh, Pd, Hf, Ta, W, Os, Ir, and Au) introduced into Ti-ATA (ATA = 2-aminoterephthalic acid) for the photocatalytic reduction of CO_2 to C_2 products. CO_2 can be sufficiently activated on Ti(M)-ATA but the adsorption configuration depends on the nature of M. Over Ti(Nb)-ATA, Ti(Ta)-ATA, Ti(Zr)-ATA and Ti(Hf)-ATA, the two *CHO species undergo C–C coupling to form *CHOCHO, an important C_2 intermediate. Ti(Nb)-ATA and Ti(Ta)-ATA tend to generate ethanol, while Ti(Zr)-ATA and Ti(Hf)-ATA are more selective to ethylene. Among the Ti(M)-ATA candidates studied, Ti(Nb)-ATA was identified as the most active catalyst for CO_2 reduction to ethanol due to its smallest limiting free energy change (1.12 eV), over which the $*CH_2CH_2O$ reduction to $*CH_2CH_2OH$ was found to be the rate-determining step. The correlation curve analysis illustrates that the reduction activity of Ti(M)-ATA catalysts is highly dependent on the binding strength of CO_2 and key reaction intermediates such as *OCHOH. The analysis of electronic and optical properties indicates that the altered energy band structure and charge transfer behavior around the bimetallic nodes of Ti(Nb)-ATA account for its excellent catalytic activity for CO_2 reduction to ethanol.

Received 30th April 2025
Accepted 22nd July 2025

DOI: 10.1039/d5ta03415a

rsc.li/materials-a

1 Introduction

The utilization of fossil fuels for the production of various industrial products emits large amounts of carbon dioxide (CO_2) into the atmosphere, leading to serious environmental problems.[1,2] Coping with these challenges, catalytic conversions of CO_2 into valuable chemicals *via* sustainable strategies offer promising approaches.[3,4] Photocatalytic reduction driven by renewable solar energy can convert CO_2 into liquid fuels and value-added chemicals such as ethanol, olefins, and carboxylic acids, which is widely recognized as a sustainable and green approach for CO_2 conversion.[5–7] Photocatalytic reduction of CO_2 to C_2 chemicals is economically more valuable and the process involves multi-electron transfer and multi-proton activation processes. However, the insufficient interactions of CO_2 molecules with the active sites of catalysts, the difficulty of CO_2 activation, and retarded C–C coupling kinetics lead to the limited formation of C_2 products with lower selectivity and yields.[8] Therefore, the rational design of highly efficient and selective photocatalysts with multi-functional active sites to exert synergistic effects is urgently desired to tune the catalytic activity and selectivity to C_2 products.

Over the past few years, a new class of semiconductor-like crystalline porous materials known as metal–organic frameworks (MOFs) has attracted increasing attention in the fields of heterogeneous catalysis, gas storage, and separation.[9,10] MOFs are composed of inorganic metal ions and organic ligands, featuring well-defined structures, high porosity, larger surface area, component diversity, and tailorability.[11] Therefore, MOF-based materials possess rich physicochemical properties and unique structural advantages among porous catalytic materials. In particular, the large surface areas and specially designed active sites of MOFs could enrich CO_2 efficiently with superior CO_2 adsorption capacity and stabilize the reaction intermediates, making them promising platforms for the photocatalytic reduction of CO_2 to chemicals and fuels.[12,13]

However, only a limited number of MOF-based photocatalytic systems have been developed for CO_2 reduction and their efficiency to C_2 products is still far from satisfactory. Enhancing the photocatalytic efficiency of MOFs for C_2 formation mainly depends on their ability to generate and maintain photogenerated electrons as well as their ability to activate CO_2 and accelerate C–C coupling.[14] Over the past decade, researchers have designed strategies to improve the photocatalytic performance of MOFs, as summarized below:

[a]State Key Laboratory of Fine Chemicals, Frontier Science Center for Smart Materials, PSU-DUT Joint Center for Energy Research, School of Chemical Engineering, Dalian University of Technology, Dalian 116024, China. E-mail: niexiaowa@dlut.edu.cn; guoxw@dlut.edu.cn

[b]Department of Chemistry, Faculty of Science, The Chinese University of Hong Kong, Shatin, NT, Hong Kong 999077. E-mail: chunshansong@cuhk.edu.hk

† Electronic supplementary information (ESI) available: Fig. S1–S8 and Tables S1–S4. See DOI: https://doi.org/10.1039/d5ta03415a

‡ These authors contributed equally to this work.

(1) By constructing efficient active sites and using the chelating effect of ligands to immobilize atomically dispersed single/dual metals, the photocatalytic reaction can be promoted.[15–17] For example, our group successfully synthesized a novel Ti-based MOF photocatalyst denoted as Fe/Ti-BPDC (BPDC = 2,2′-bipyridine-5,5′-dicarboxylic acid) with atomically dispersed Fe sites, which exhibited high activity and selectivity for CO_2 reduction to HCOOH, with a yield of 703.9 μmol g^{-1} h^{-1} and a selectivity greater than 99.7%.[18] Inspired by the experimental work, we proposed a new strategy for designing metal single-atom-modified and dual-atom-modified Ti-BPDC photocatalysts through structural and electronic modulation for CO_2 reduction to C_1 and C_2 products using density functional theory (DFT) calculations.[19,20] The computational results of structure–activity volcano curves show that metal single-atom modified Fe/Ti-BPDC ($\Delta G_L = 0.40$ eV) and Pd/Ti-BPDC ($\Delta G_L = 1.17$ eV) are optimal catalysts for the photoreduction of CO_2 to HCOOH and CH_3OH, respectively,[19] due to their relatively small limiting free energy changes compared to those reported in the literature.[21] Furthermore, metal dual-atom-modified Ti-BPDCs such as Cu–Sn/Ti-BPDC ($\Delta G_L = 0.20$ eV) and Cu–Os/Ti-BPDC ($\Delta G_L = 0.70$ eV) show enhanced activity toward the generation of HCOOH and CH_3OH products from CO_2 photoreduction compared to metal single-atom modified Fe/Ti-BPDC and Pd/Ti-BPDC. In particular, the dual-metal atom-modified Cu–In/Ti-BPDC ($\Delta G_L = 1.37$ eV) exhibits improved activity and selectivity towards the generation of C_2 products (mainly C_2H_4).[20]

(2) Light absorption efficiency can be improved by choosing the right ligands. For example, in order to improve the optical properties of MIL-125 (Ti) MOFs, researchers successfully shifted MIL-125 (Ti) to the visible range by introducing the 2-aminoterephthalic acid (ATA) ligand with a broad spectral response, enhancing the visible light absorption of the MOF materials.[22] Sun *et al.* reported that MIL-125-NH_2(Ti) with {110}/{111}-heterojunction yields 10 and 18 times more CO and CH_4 products, respectively, from CO_2 photoreduction compared with the single {001} facet; DFT calculations identified energetically favorable pathways and rate-limiting steps for CO_2 reduction on different low-index surfaces of MIL-125-NH_2(Ti) in their studies.[23]

(3) In addition, metal substitution/doping has been demonstrated to be an effective method to improve the performance of MOF-based photocatalysts. One of the effective strategies is to construct bimetallic assemblies by partially replacing a node metal in MOFs with another metal. The bimetallic assemblies can harvest visible light and the doped metal cations can act as electronic mediators to promote charge transfer, facilitating the photocatalytic processes.[24] In particular, partial substitution of metal cations in MOFs can lead to the formation of oxygen-bridged heterometallic structures within the framework, which could exhibit enhanced photocatalytic performance due to the structural flexibility and tunability of the designed MOFs.[25] For example, Ti-substituted NH_2-UiO-66 (Zr/Ti) was prepared by Li *et al.* by using the post-synthesis exchange (PSE) method which exhibits good catalytic performance for the photoreduction of CO_2 to formic acid under visible light, with a yield of 5.8 mmol mol^{-1} for 10 h; DFT calculations and electron spin resonance (ESR) results indicate that the introduction of Ti substituents as a mediator promotes electron transfer, which improves the photocatalytic performance.[25] In addition, Truhlar *et al.* used UiO-66 as the basic skeleton and replaced partial Zr atoms in the nodes with metals such as Hf, Th, Ti, U, Ce, *etc.*; DFT calculations show that UiO-66(Ce) effectively promotes electron–hole separation due to the fact that Ce^{4+} in the material has a low-energy 4f vacancy orbital, which can receive photogenerated electrons, thus more effectively driving the photocatalytic reaction.[26]

Based on the literature survey and prior studies in our group, the structures and properties of ligands in MOF materials have important impacts on the photocatalytic performance of CO_2 reduction. On the one hand, metal single-atom and dual-atom assemblies can be stably anchored with N-containing ligands within the MOF framework to improve the efficiency of CO_2 activation and conversion.[18–20,27] On the other hand, metal-modified nodes can effectively regulate light absorption and electron–hole separation efficiency, and provide special active sites to further tune the activity and selectivity of MOF-based catalysts for CO_2 photoreduction.[25,26,28] However, the directional control of CO_2 reduction products remains challenging, especially for the generation of C_2 products. Due to the complex mechanisms of adsorption/activation of CO_2 and cleavage/reconstruction of C=O double bonds over the active sites of catalysts, the principles governing the formation and transformation of key intermediates and electron–proton transfer in the reaction processes are still not clear, which make it difficult to regulate the conversion paths and target products.

The limited efficiency of MOF-based photocatalysts in the reduction of CO_2 to C_2 products (*e.g.*, ethanol and ethylene) stems from several intrinsic challenges, among which insufficient activation of CO_2, slow kinetics of C–C coupling, and generation of key intermediates required for C–C coupling are the major bottlenecks.[29] On the one hand, many MOFs lack robust adsorption sites (*e.g.*, metal active sites or Lewis base sites) to activate the linear structure of CO_2, which prevents the reduction of CO_2 to the critical *HCOO or *COOH intermediate. On the other hand, C_2 product generation requires multiple electrons, but MOFs usually lack efficient charge transport channels to deliver electrons quickly. In addition, the lack of bimetallic site nodes in some MOF materials leads to low stability of C–C coupling intermediates. To summarize, the synergistic optimization of CO_2 adsorption/activation, electron transfer, intermediate stability, and C–C coupling kinetics inside MOF materials is a crucial factor in overcoming the inefficiency of MOF-based photocatalysts for the production of C_2 products.

Inspired by our previous experimental studies on Ti-based MOFs and the potential application of 2-aminoterephthalic acid (ATA) ligands in MOFs for photocatalysis,[30,31] the present work systematically investigates the adsorption/activation and reduction of CO_2 to C_2 products (mainly ethanol and ethylene) on a series of metal node-modified Ti(M)-ATA MOFs (ATA = 2-aminoterephthalic acid, M = Mn, Fe, Co, Ni, Cu, Zn, Zr, Nb, Mo, Ru, Rh, Pd, Hf, Ta, W, Os, Ir, Au) by means of DFT calculations. By screening these heterometallic node structures *via* structure–activity correlation, Ti(Nb)-ATA is identified as the most active photocatalyst for CO_2 reduction to ethanol (C_2H_5OH), with

a limiting free energy change of 1.12 eV associated with the $*CH_2CH_2O \rightarrow *CH_2CH_2OH$ step. Electronic property analysis further demonstrates that the computationally designed Ti(Nb)-ATA MOF catalyst *via* node modification is more favorable for the photocatalytic reduction of CO_2 to C_2 compared to unmodified Ti-ATA and other Ti-based MOFs such as Ti/BPDC and MIL-125-NH_2(Ti). In addition, we also find that node-modified metals from different groups of the periodic table lead to different C_2 products. For example, Ti(Ta)-ATA and Ti(Nb)-ATA tend to generate ethanol, while Ti(Zr)-ATA and Ti(Hf)-ATA are more selective to ethylene.

2 Computational models and methods

The present work builds on recent experimental studies by He *et al.* in our group, where characterization by X-ray diffraction (XRD) showed that the synthesized Ti-BPDC (BPDC = 2,2′-bipyridine-5,5′-dicarboxylic acid) has high crystallinity; the Ti and O atoms are periodically aligned to form Ti–O layers, and the Ti–O layers connected to the organic ligand are parallel to each other.[18,30] To construct the computational models in this work, we chose 2-aminoterephthalic acid (ATA) as the linker instead of BPDC and the aforementioned Ti-MOF as the basic framework. Within the constructed Ti-MOF catalyst, the Ti and O atoms in the nodes of the MOF exhibit periodically arranged Ti–O layers, with each Ti atom connected to six O atoms to form Ti–O clusters, in which two of the O atoms belong to the ATA linker and four of the O atoms are from the Ti–O layers, as shown in Fig. 1(a) and (c). A periodic cell of Ti-ATA-based MOFs with a lattice constant of 6.44 Å × 21.75 Å × 7.40 Å was built for modelling (Fig. 1(a)). Then, representative metals including Mn, Fe, Co, Ni, Cu, Zn, Zr, Nb, Mo, Ru, Rh, Pd, Hf, Ta, W, Os, Ir, and Au were selected as doping metals for node modification (denoted as Ti(M)-ATA (Fig. 1(b)). According to the literature, bimetallic assemblies with Ti–O–M oxygen-bridged structures are formed in typical Ti-ATA MOF materials through metal substitution in the modification processes.[25] Here, upon introducing the second metal atoms into Ti-ATA, two possible configurations were considered, *i.e.* one is the formation of a Ti–Ti diagonal structure in one parallelogram at the node center which separates the second metal atoms into different parallelograms, and the other is the formation of an M–M diagonal structure in one parallelogram at the node center within the MOF, separating the Ti atoms into different parallelograms, as illustrated in Fig. 1(d).

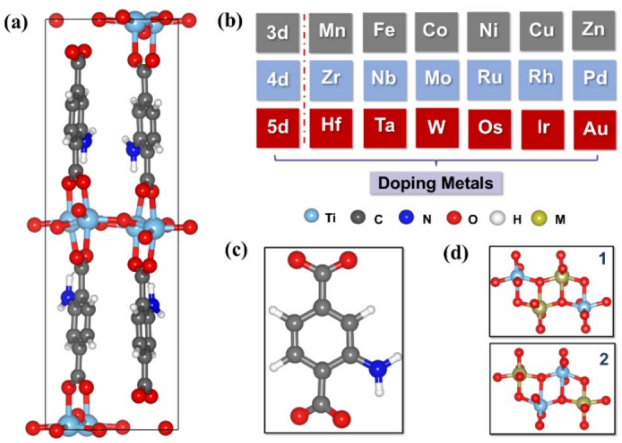

Fig. 1 (a) The optimized structure of the Ti-ATA (ATA = 2-amino-terephthalic acid) framework. (b) Representative 3d (Mn, Fe, Co, Ni, Cu, and Zn), 4d (Zr, Nb, Mo, Ru, Rh, and Pd), and 5d (Hf, Ta, W, Os, Ir, and Au) metals selected as doping metals for node modification in Ti(M)-ATA catalysts. (c) Structure of the 2-aminoterephthalic acid (ATA) linker. (d) Two possible node configurations formed in Ti(M)-ATA catalysts.

An all-electronic approach implemented in the Vienna *Ab initio* Simulation Package (VASP) program was used to perform spin-polarized DFT calculations.[32,33] The projector-augmented wave (PAW) pseudopotentials were used to describe the electron–ion interactions. The Perdew–Burke–Ernzerhof (PBE) functional in the generalized gradient approximation (GGA) was used to calculate the exchange–correlation energies of electrons.[34] The Coulomb and exchange interactions were corrected by setting the U_{eff} parameter (U_{eff} = Coulomb U − exchange J) for each transition metal.[35,36] The U_{eff} parameter for titanium atom was set to 3.0 eV, and those for remaining metals are given in Table S1 in the ESI.† To include van der Waals (vdW) interactions, the PBE + D3 method was used.[37,38] The valence electrons were described using a plane wave basis set with a cutoff energy of 450 eV. The convergence criteria for all calculated electronic energies and atomic forces were set to 10^{-4} eV and 0.03 eV $Å^{-1}$, respectively. Both Ti-ATA and Ti(M)-ATA structures were optimized using a 4 × 1 × 4 *k*-point mesh for sampling the Brillouin zone in the VASP calculations.

The adsorption energy (E_{ads}) of an adsorbate onto the catalyst was calculated using the equation $E_{ads} = E_{total} - E_{catalyst} - E_{adsorbate}$, where E_{total}, $E_{catalyst}$, and $E_{adsorbate}$ represent the total energy of the system containing the adsorbate and catalyst, the energy of the bare catalyst, and the energy of the adsorbate in the gas phase, respectively. In order to evaluate the catalytic activity of CO_2 photoreduction over these Ti(M)-ATA catalysts, the free energy change (ΔG) was calculated for each elementary step involved in the CO_2 reduction process using the formula $\Delta G = \Delta E + \Delta E_{ZEP} - T\Delta S$,[39,40] where ΔE is the total electronic energy change obtained through DFT calculations, ΔE_{ZEP} is the zero-point energy contribution, T is the temperature at 298. 15 K, and ΔS is the entropy change. The zero-point energy and entropy were obtained from vibrational frequency calculations using DFT. The zero-point energies of all adsorbed species are provided in Table S2.† In this work, we investigated the reaction pathways for the formation of different C_2 products (mainly C_2H_4 and C_2H_5OH) over Ti-ATA and Ti(M)-ATA catalysts, in which protons and photogenerated electrons are added to the reaction intermediates progressively in the presence of a catalyst, ultimately resulting in the formation of C_2 products.

3 Results and discussion

3.1 Structural stability of Ti(M)-ATA catalysts and the adsorption of CO_2

For clarity, we grouped the introduced second metals (M) into three categories based on their d electrons as 3d (Mn, Fe, Co, Ni,

Cu, and Zn), 4d (Zr, Nb, Mo, Ru, Rh, and Pd), and 5d (Hf, Ta, W, Os, Ir, and Au). Before exploring the adsorption of CO_2 molecules on the designed Ti(M)-ATA catalysts, we first investigated the structural stabilities of the two types of metal-modified nodes of MOFs (Fig. 1(d)). The calculated DFT energies are presented in Fig. S1,† and the results show that Ti(M)-ATA candidates, except Ti(Zn)-ATA, exhibit a periodic enhancement of DFT energies from left to right according to the periodic table of elements. Notably, the absolute energy values of these two different node configurations are not very different. Therefore, we further calculated the substitution energies of bimetallic assemblies in Ti(M)-ATA as shown in Fig. S2,† and the specific values are given in Table S3.† The results show that considerable negative substitution energies are obtained for Ti(M)-ATA (M = Zr, Nb, Hf, Ta), which range from −0.93 eV to −3.70 eV. However, all other candidate catalysts have positive substitution energy values, indicating that Zr, Nb, Hf, and Ta atoms can bind strongly to the node Ti atom in the MOFs, thus ensuring their high structural stability.

It is worth noting that DFT energy and substitution energy alone are not sufficient to determine the optimal doping model for metal modification. Therefore, we further explored all possible adsorption configurations of CO_2 on the two different node models, considering four different initial adsorption configurations, including *COO, *OCO, O*CO, and O*OC (* indicates adsorption at the doped metal active site). With model structure 1, as shown in Fig. 1(d), after comprehensive structural screening and optimization, it was found that CO_2 is adequately activated on Ti(M)-ATA (M = Nb, Zr, Ta, Hf), with one O atom of CO_2 bonded to the doped metal site in the node and the C atom of CO_2 bonded with the N atom in the ATA ligand, forming a stable *O(M)–C(N)–O angular adsorption structure, as shown in Fig. 2(a). However, on the catalyst models of Ti(M)-ATA (M = Mn, Fe, Co, Ni, Cu, Zn, Mo, Ru, Rh, Pd, W, Os, Ir, Au), CO_2 shows a linear adsorption configuration and is not bonded to other atoms in the MOF catalysts, as illustrated in Fig. S3.† With model structure 2 as shown in Fig. 1(d), CO_2 exhibits the *O(Zr)–C(N)–O adsorption mode merely on Ti(Zr)-ATA whereas it shows a linear adsorption pattern on the rest of the candidate catalysts, as shown in Fig. S4.† The adsorption energies of CO_2 on pristine Ti-ATA and metal-modified Ti(M)-ATA (model structure 1 and model structure 2) were calculated, as shown in Fig. 2(b–d) and S5,† while the specific values of adsorption energies are provided in Table S4.† The calculation results show that the adsorption energy values of CO_2 on Ti(M)-ATA (M = Nb, Zr, Ta, Hf) are 0.15, 0.31, −0.10, and 0.26 eV, respectively, which are significantly lower than that obtained over the pristine Ti-ATA catalyst (1.45 eV) and those obtained over other metal-modified Ti(M)-ATA candidate catalysts. Therefore, the Ti(M)-ATA (M = Nb, Zr, Ta, Hf) candidates were chosen for subsequent exploration of the reaction pathways and reactivities for CO_2 photoreduction to C_2 products. It is worth noting that the adsorption energies of CO_2 on model structure 1 are generally lower than those on model structure 2, as shown in Fig. S5.† Based on the calculated CO_2 adsorption configurations and adsorption energies, the metal-modified

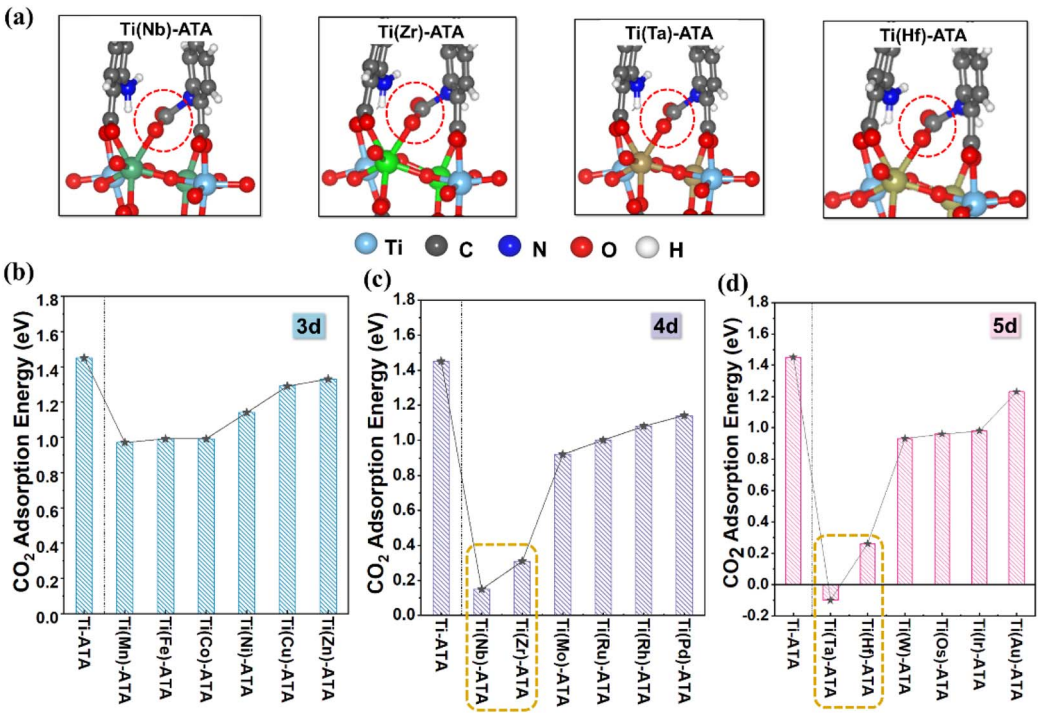

Fig. 2 (a) The optimized stable adsorption configurations of CO_2 molecules on metal-modified model structure 1 of Ti(M)-ATA (M = Nb, Zr, Ta, Hf); (b) the adsorption energies of CO_2 on pristine Ti-ATA and metal-modified model structure 1 of Ti(M)-ATA (M = Mn, Fe, Co, Ni, Cu, Zn); (c) the adsorption energies of CO_2 on pristine Ti-ATA and metal-modified model structure 1 of Ti(M)-ATA (M = Zr, Nb, Mo, Ru, Rh, Pd); (d) the adsorption energies of CO_2 on pristine Ti-ATA and metal-modified model structure 1of Ti(M)-ATA (M = Hf, Ta, W, Os, Ir, Au).

model structure 1 exhibits good structural stability, sufficient interactions with CO_2, and better ability to activate CO_2; therefore it was chosen as the representative node-modification model for subsequent studies.

3.2 CO_2 reduction mechanisms and catalytic performance of Ti-ATA and Ti(M)-ATA (M = Zr, Nb, Hf, Ta)

Since CO_2 can be sufficiently activated on Ti(M)-ATA (M = Zr, Nb, Hf, Ta), we proceeded to investigate the reaction properties of CO_2 reduction over these candidate catalysts. The reduction of CO_2 to C_2 products can be divided into hydrogenation processes and C–C coupling reaction. In particular, the formation of stable C–C coupling intermediates on the catalyst is a crucial step in the reduction of CO_2 to C_2 products; thus we first examined all possible hydrogenation pathways for CO_2 reduction before C–C coupling on pristine Ti-ATA and metal-modified Ti(M)-ATA (M = Zr, Nb, Hf, Ta) candidates, and mapped out the Gibbs free energy diagrams as shown in Fig. 3. The first proton may attack the O or C atom of *OCO, forming the *OCOH or *OCHO intermediate, respectively. For the IVB metals in the periodic table, including single metal Ti, bi-metal Ti(Zr) and Ti(Hf), the *OCOH intermediate cannot be stabilized even after structural optimization and spontaneously transforms into the *OCHO intermediate. Moreover, it is found that the first hydrogenation step of *OCO → *OCHO is thermodynamically quite unfavorable on Ti (Zr) and Ti (Hf), with ΔG values of 0.91 and 1.18 eV, respectively, as shown in Fig. 3(b) and (c). Although the hydrogenation of *OCO to the *OCHO intermediate is slightly uphill (ΔG of 0.17 eV) over pristine Ti-ATA, the CO_2 adsorption/activation process is largely endothermic (ΔG of 1.45 eV) on this catalyst, as illustrated in Fig. 3(a). In the next scenario, the continued hydrogenation of *OCHO to form the *OCHOH species is significantly exothermic, releasing energies of 2.92, 2.77, and 2.81 eV, respectively on Ti-ATA, Ti(Zr)-ATA, and Ti(Hf)-ATA. Then, the formed *OCHOH species needs to overcome large uphill energy barriers (ΔG = 1.48, 2.04, and 2.10 eV on Ti-ATA, Ti(Zr)-ATA, and Ti(Hf)-ATA) to dissociate into the key *CHO intermediate species, releasing a H_2O molecule simultaneously. Overall, the formation of the key *CHO intermediate on Ti-ATA, Ti(Zr)-ATA, and Ti(Hf)-ATA is quite energy consuming and thus energetically unfavorable. By contrast, for the VB metals including Ti(Nb) and Ti(Ta), both intermediates can be formed from the first hydrogenation step of *OCO. Clearly, the *OCHO intermediate is much more stable than the *OCOH intermediate, as illustrated in Fig. 3(d) and (e); thus the pathway for further conversion of the *OCOH intermediate is not considered here. Subsequently, the hydrogenation of the *OCHO intermediate on Ti(Nb)-ATA and Ti(Ta)-ATA requires overcoming moderate uphill energies of 0.68 and 0.72 eV, respectively, leading to the formation of the *OCHOH intermediate. In the next step, the continued reduction of *OCHOH on Ti(Nb)-ATA to form the key intermediate *CHO is thermodynamically favorable, releasing an energy of 0.71 eV, whereas the formation of *CHO species on Ti(Ta)-ATA still requires overcoming an energy barrier of 0.35 eV. The above calculation results reveal that the formation of the key *CHO intermediate is thermodynamically more preferred on the Ti(Nb)-ATA catalyst, which plays an important role in subsequent C–C coupling and further reduction to generate C_2 products.

Starting with the formed *CHO species, all possible pathways and intermediates for the reduction of CO_2 to C_2H_4 or C_2H_5OH products on pristine Ti-ATA and metal-modified Ti(M)-ATA (M = Zr, Hf, Nb, Ta) were considered, as illustrated in Fig. 4. By comparing the reaction Gibbs free energies, the optimal pathway for CO_2 reduction to C_2H_4 or C_2H_5OH over each of the examined catalyst was identified, as shown in Fig. 5(a) and (b), and the optimized structures of relevant

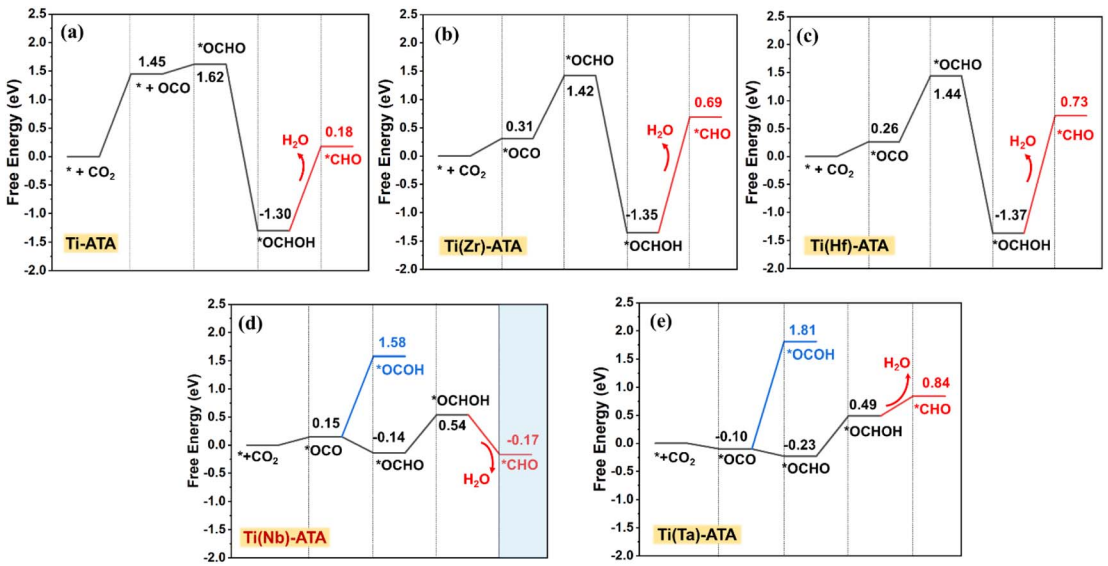

Fig. 3 The calculated Gibbs free energy diagrams for CO_2 reduction steps before C–C coupling on (a) Ti-ATA, (b) Ti(Zr)-ATA, (c) Ti(Hf)-ATA, (d) Ti(Nb)-ATA, and (e) Ti(Ta)-ATA catalysts.

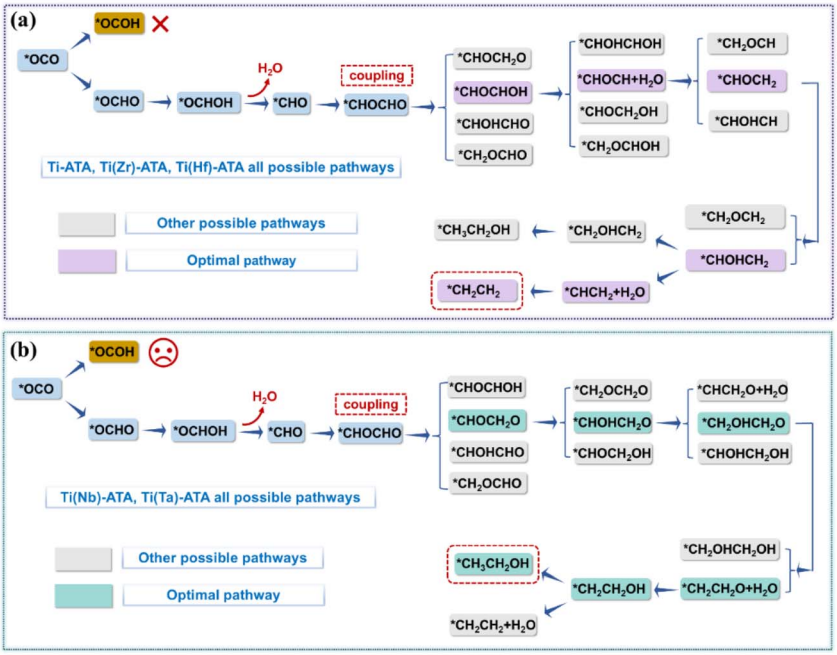

Fig. 4 Possible reaction pathways considered for the reduction of CO_2 to C_2 (C_2H_5OH and C_2H_4) products on (a) Ti-ATA, Ti(Zr)-ATA, and Ti(Hf)-ATA and (b) Ti(Nb)-ATA and Ti(Ta)-ATA.

intermediates are given in Fig. 5(c) and (d). Other pathways considered and investigated are provided in Fig. S6.† In this scenario, we focus on discussing the reaction mechanisms starting from the C–C coupling step, as detailed below:

(1) According to the free energy diagram shown in Fig. 5(a), over pristine Ti-ATA, metal-modified Ti(Zr)-ATA and Ti(Hf)-ATA, the two *CHO species undergo C–C coupling to form the important C_2 intermediate *CHOCHO (Fig. 5(b)), releasing the energies of 0.98, 1.91, and 1.99 eV, respectively on the three catalysts. The subsequent conversion of *CHOCHO species leads to the formation of four possible intermediates, namely *CHOCHOH, *$CHOCH_2O$, *CHOHCHO, or *CH_2OCHO. The calculated Gibbs free energies in Fig. S6(a–c)† show that the formation of these four intermediates is thermodynamically unfavorable due to the uphill free energy changes, with the *CHOCHOH species formation involving a relatively smaller

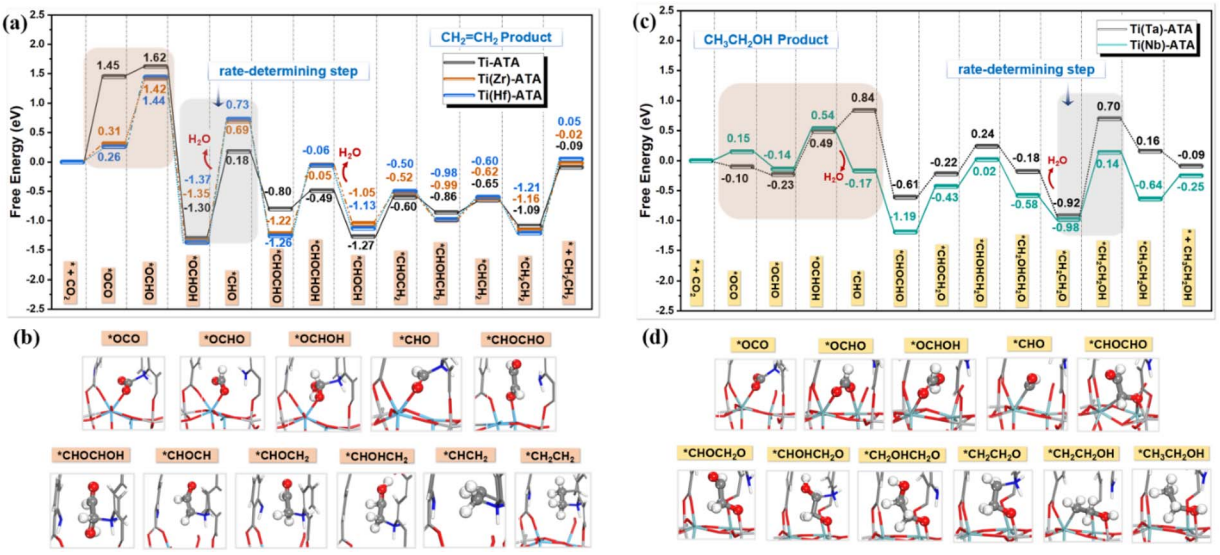

Fig. 5 The calculated Gibbs free energy diagrams of the optimal paths for CO_2 reduction to the C_2H_4 product on (a) Ti-ATA, Ti(Zr)-ATA, and Ti(Hf)-ATA and to the C_2H_5OH product on (c) Ti(Nb)-ATA and Ti(Ta)-ATA. Structural illustrations of all stable intermediates associated with the optimal pathways on (b) Ti-ATA, Ti(Zr)-ATA, and Ti(Hf)-ATA and (d) Ti(Nb)-ATA and Ti(Ta)-ATA. The MOF framework structure is omitted for clarity.

energy increase compared to the other three species ($\Delta G = 0.31$ (Ti-ATA), 1.17 (Ti(Zr-ATA)), and 1.20 eV (Ti(Hf)-ATA)). The formed *CHOCHOH intermediate is then reduced by proton-coupled electron transfer to form *CHOHCHOH, *CHOCH + H_2O, *$CHOCH_2OH$, or *CH_2OCHOH species. Notably, the ΔG values for the formation of *CHOCH + *H_2O on Ti-ATA, Ti(Zr)-ATA, and Ti(Hf)-ATA are −0.78, −1.00, and −1.07 eV, respectively, which are lower than those for the formation of the other three intermediates (Fig. S6(a–c)†), suggesting that *CHOCH + *H_2O is the preferred intermediate from *CHOCHOH reduction. In the next step, further reduction of *CHOCH leads to the formation of *CH_2OCH, *$CHOCH_2$, or *CHOHCH. As demonstrated in Fig. 5(a) and S6(a–c),† the formation of *CH_2OCH, *$CHOCH_2$, and *CHOHCH species is thermodynamically unfavorable due to uphill free energy changes, but *$CHOCH_2$ is relatively more stable than the other two species, with ΔG values of 0.67 (Ti-ATA), 0.53 (Ti(Zr)-ATA), and 0.63 eV (Ti(Hf)-ATA), respectively. Subsequently, the *$CHOCH_2$ intermediate undergoes further reduction to either *CH_2OCH_2 or *$CHOHCH_2$ species, with the formation of *$CHOHCH_2$ species being thermodynamically more favorable, as shown in Fig. S6(a–c).† In contrast, the reduction of *$CHOCH_2$ to *CH_2OCH_2 species is thermodynamically unfavorable, with ΔG values of −0.26 (Ti-ATA), −0.47 (Ti(Zr)-ATA), and −0.48 eV (Ti(Hf)-ATA), as shown in Fig. 5(a). For the generated *$CHOHCH_2$ intermediate, two possible hydrogenation pathways lead to different C_2 intermediates: either the formation of *$CHCH_2$ species by releasing a H_2O molecule ($\Delta G = 0.21$ (Ti-ATA), 0.37 (Ti(Zr)-ATA), and 0.38 eV (Ti(Hf)-ATA)), which is then reduced to *CH_2CH_2 ($\Delta G = -0.44$ (Ti-ATA), −0.54 (Ti(Zr)-ATA), and −0.61 eV (Ti(Hf)-ATA)), or the generated *$CHOHCH_2$ intermediate continues to be hydrogenated to form *CH_2OHCH_2 species which is further reduced to *CH_2OHCH_3. Finally, the formed *CH_2OHCH_3 (*C_2H_5OH) or *CH_2CH_2 (*C_2H_4) desorbs from the catalysts. Apparently, the reduction of CO_2 to *C_2H_4 over Ti-ATA, Ti(Zr)-ATA, and Ti(Hf)-ATA catalysts is more selective (energetically favorable) than to *C_2H_5OH according to the calculation results given in Fig. S6(a–c).† However, the desorption of formed *CH_2CH_2 from the catalyst proceeds slowly due to the substantial free energy changes on the three catalysts examined, as shown in Fig. 5(a). Based on the above results, the optimal pathway for the photocatalytic reduction of CO_2 to the preferred C_2H_4 product on pristine Ti-ATA, metal-modified Ti(Zr)-ATA and Ti(Hf)-ATA catalysts can be summarized as *CO_2 → *OCHO → *OCHOH → *CHO → *CHOCHO → *CHOCHOH → *CHOCH + H_2O → *$CHOCH_2$ → *$CHOHCH_2$ → *$CHCH_2$ → *CH_2CH_2 → *+C_2H_4. According to the free energy diagram in Fig. 5(a), the reduction step *OCHOH → *CHO ($\Delta G = 1.48$ (Ti-ATA), 2.04 (Ti(Zr)-ATA), and 2.10 eV (Ti(Hf)-ATA)) has the largest free energy change and is considered to be the rate-determining step for the overall reaction. On these three catalysts, C–C coupling is not difficult to achieve with a substantially downhill free energy change; however the hydrogenation reactions before C–C coupling proceed slowly, especially the generation of the key *CHO intermediate.

(2) In contrast, the mechanisms of CO_2 reduction to C_2 products on Ti(Nb)-ATA and Ti(Ta)-ATA catalysts are different. According to the free energy diagrams given in Fig. 5(c), for Ti(Nb)-ATA and Ti(Ta)-ATA, the two *CHO species undergo C–C coupling to form *CHOCHO (Fig. 5(d)), an important C_2 intermediate, releasing the energies of 1.02 and 1.45 eV, respectively on the two catalysts. Further reduction of *CHOCHO species proceeds *via* different pathways. As illustrated in Fig. S6(d) and (e),† among the four possible intermediates produced from *CHOCHO reduction, the formation of *$CHOCH_2O$ is thermodynamically the most favorable, with ΔG values of 0.45 and 0.46 eV, on Ti(Nb)-ATA and Ti(Ta)-ATA, respectively. The formed *$CHOCH_2O$ species can be further reduced to *CH_2OCH_2O, *$CHOHCH_2O$ or *$CHOCH_2OH$. From Fig. S6(d) and (e),† it can be seen that *$CHOHCH_2O$ formation has a lower Gibbs free energy change compared to *CH_2OCH_2O and *$CHOCH_2OH$. In the next step, the formed *$CHOHCH_2O$ species can be further reduced to three possible intermediates including *CH_2OHCH_2O, *$CHCH_2O$ + H_2O or *$CHOHCH_2OH$. Based on the Gibbs free energy diagrams given in Fig. 5(c) and S6(d), (e),† it can be observed that the formation of the *CH_2OHCH_2O intermediate is thermodynamically much more favorable ($\Delta G =$ −0.60 (Ti(Nb)-ATA) and −0.42 eV (Ti(Ta)-ATA)), whereas the formation of *$CHCH_2O$ + H_2O and *$CHOHCH_2OH$ intermediates is associated with large free energy barriers. Subsequently, the resulting *CH_2OHCH_2O species can either be reduced to *CH_2OHCH_2OH species which is thermodynamically unfavorable, or to *CH_2CH_2O and a H_2O molecule which is thermodynamically favorable. The ΔG values for *CH_2OHCH_2O reduction to *CH_2CH_2O + *H_2O on Ti(Nb)-ATA and Ti(Ta)-ATA are calculated to be 0.40 and 0.74 eV, respectively. After the release of H_2O molecule, the remaining *CH_2CH_2O species can be further reduced by proton coupled electron transfer to produce the *CH_2CH_2OH species. As shown in Fig. 5(b), remarkably, the Gibbs free energy change for this hydrogenation process increases by 1.12 and 1.62 eV for Ti(Nb)-ATA and Ti(Ta)-ATA, respectively. In the last step, further reduction of *CH_2CH_2OH generates either *CH_2CH_2 + H_2O or *CH_3CH_2OH. Unlike Ti-ATA, Ti(Zr)-ATA, and Ti(Hf)-ATA, it is clear that the generation of *CH_3CH_2OH (*C_2H_5OH) on Ti(Nb)-ATA and Ti(Ta)-ATA is energetically more favorable than the formation of *CH_2CH_2 (*C_2H_4), as shown in Fig. S6(d) and (e),† and the corresponding ΔG values for *C_2H_5OH formation on these two catalysts are −0.78 and −0.54 eV, respectively. It is worth noting that there is a small uphill energy change involved in the desorption of *CH_3CH_2OH species on Ti(Nb)-ATA; however, the *CH_3CH_2OH desorption is not a highly energy-consuming step compared to the preceding step of *CH_2CH_2O reduction to *CH_2CH_2OH with a large positive ΔG value, as illustrated in Fig. 5(c). To sum up, for the reduction of CO_2 to the preferred C_2H_5OH product on Ti(Nb)-ATA and Ti(Ta)-ATA catalysts, the optimal pathway is identified as *CO_2 → *OCHO → *OCHOH → *CHO → *CHOCHO → *$CHOCH_2O$ → *$CHOHCH_2O$ → *CH_2OHCH_2O → *CH_2CH_2O + H_2O → *CH_2CH_2OH → *CH_3CH_2OH → *+C_2H_5OH, in which the rate-determining step is found to be the reduction of *CH_2CH_2O → *CH_2CH_2OH as it

involves the highest free energy change ($\Delta G = 1.12$ (Ti(Nb)-ATA) and 1.62 eV (Ti(Ta)-ATA)) among all of the elementary steps.

Moreover, we also calculated the kinetic barrier of the rate-determining step in the optimal energy pathway for CO_2 reduction to ethanol on Ti(Nb)-ATA and Ti(Zr)-ATA, as shown in Fig. S7.† In addition to considering the energy barrier of the rate-determining step, the corresponding reaction rate constant was also calculated and is provided in Table S5.† The results show that the CO_2 reduction has an obvious kinetic advantage on Ti(Nb)-ATA compared to Ti(Zr)-ATA based on both the Gibbs free energy barrier and reaction rate constant calculations, further consolidate the above screening results.

Since the adsorption and activation of CO_2 is an extremely important initial step in CO_2 reduction, as demonstrated in the previous studies,[19,20,41] here we correlated the adsorption energy of CO_2 with the limiting free energy change for the generation of C_2 products (C_2H_4 and C_2H_5OH) on the four metal-modified Ti(M)-ATA (M = Zr, Hf, Nb, Ta) catalysts, and plotted the corresponding volcano type curve as displayed in Fig. 6(a). The calculation results show that the Ti(Nb)-ATA catalyst has the lowest limiting free energy change and a moderate CO_2 adsorption intensity, positioning it at the top of the volcano-type curve. In addition, we note that the stability of the *OCHOH intermediate affects the next step of dehydration to form the key C–C coupling intermediate of *CHO, and thus we plotted the volcano type curve of G_{*OCHOH} and the limiting free energy change on the four metal-modified Ti(M)-ATA (M = Zr, Hf, Nb, Ta) catalysts, as displayed in Fig. 6(b). The results show that the Ti(Nb)-ATA catalyst remains at the top of the volcano curve, further indicating that the moderate stability of the *OCHOH intermediate over Ti(Nb)-ATA is quite favorable for the subsequent generation of the *CHO intermediate. Therefore, the Ti(Nb)-ATA catalyst would be the best candidate for C_2 production among the four candidates studied. These results further clarify that the adsorption strength of the CO_2 reactant and key reaction intermediates (*e.g.**OCHOH) directly affects the CO_2 reduction activity, and the relatively mild bonding of $*CO_2$ and *OCHOH over Ti(Nb)-ATA is responsible for the highest activity of Ti(Nb)-ATA among the screened candidate catalysts. This finding is consistent with our previous studies on CO_2 photoreduction over other Ti-MOF-based catalytic materials.[19,20]

In addition, we note that CO_2 molecules can be adequately activated when the doped nodal metals belong to the IVB and VB groups and could provide favorable active sites for CO_2 adsorption and activation. For IVB group metal-modified Ti-ATA catalysts, such as Ti(Zr)-ATA and Ti(Hf)-ATA, CO_2 photocatalytic reduction tends to generate the C_2H_4 product and follows similar reaction pathways. In contrast, for VB group metal-modified Ti-ATA catalysts, such as Ti(Nb)-ATA and Ti(Ta)-ATA, CO_2 photoreduction to the C_2H_5OH product is energetically more preferred. The calculated limiting free energy change ($\Delta G_L = 1.12$ eV) over Ti(Nb)-ATA for C_2H_5OH generation is even smaller than that ($\Delta G_L = 1.37$ eV) over the dual metal-atom-modified Cu–In/Ti-BPDC catalyst which was identified to be a good catalyst for C_2 (C_2H_4) generation in our previous DFT work.[20] Therefore, Ti(Nb)-ATA can be proposed as a promising candidate catalyst for the photocatalytic reduction of CO_2 to C_2 products, especially C_2H_5OH. Overall, the calculation results indicate that the ATA ligand with a Ti–O–Nb dual-metal-node structure as well as with a broad absorption spectrum effectively improves the photocatalytic efficiency for CO_2 reduction to C_2 products, which are also essential for regulating the catalytic activity and product selectivity of Ti-MOF-based photocatalysts.

The CO_2 photoreduction was typically carried out in aqueous solution. Under the same conditions, *H species could be adsorbed on the active site and reduced by the proton–electron pair ($H^+ + e^-$), which would affect the photocatalytic efficiency of CO_2 reduction. Here, we calculated the Gibbs free energy diagram for the hydrogen evolution reaction (HER) on the Ti(Nb)-ATA catalyst, as shown in Fig. S8(a),† which shows that the *H species is preferentially adsorbed on the Nb atom in the node of Ti(Nb)-ATA. It is worth noting that the limiting free energy change for the HER on Ti(Nb)-ATA is calculated to be 1.29 eV, which is higher than that (1.12 eV) for CO_2 reduction;

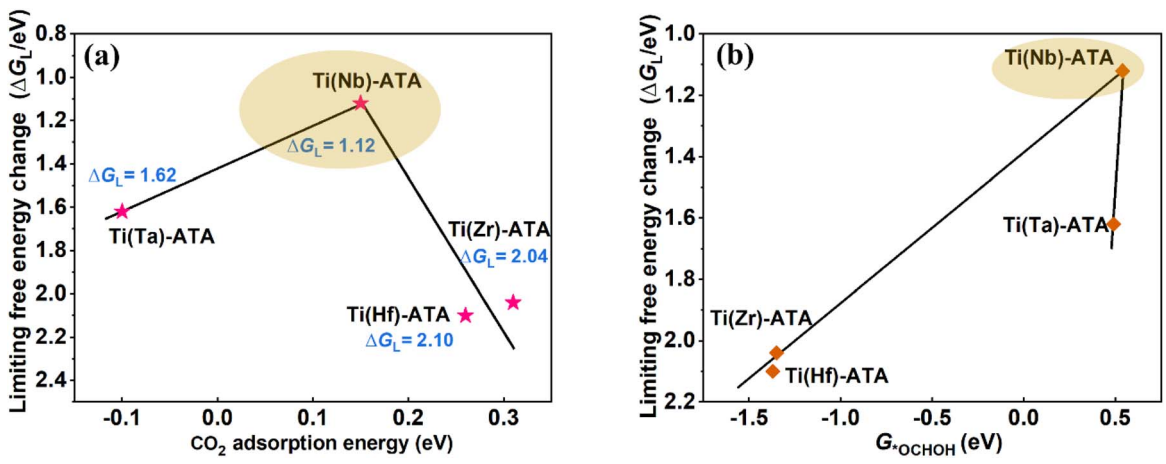

Fig. 6 Volcano-type curves between (a) CO_2 adsorption energy, (b) G_{*OCHOH} and limiting free energy change for C_2 products generation on Ti(M)-ATA (M = Zr, Hf, Nb, Ta) catalysts.

thus the competitive effect of HER is minor. In addition, we also calculated the Gibbs free energy diagrams for CO and HCOOH production from CO_2 reduction on Ti(Nb)-ATA, as shown in Fig. S8(b),† and the results show that the stability of the *CHO intermediate is higher than that of CO and HCOOH products; thus the ethanol formation pathway through the CHO* intermediate is mainly considered in this work.

3.3 Electronic structure and optical property analysis of Ti-ATA and Ti(M)-ATA (M = Zr, Nb, Hf, Ta)

In order to gain fundamental insights into the optical properties of the node-modified Ti-ATA catalysts, we further analyzed the electronic structures of pristine Ti-ATA and the best active catalyst identified, Ti(Nb)-ATA, by calculating the total and projected density of states (TDOS and PDOS) and band structures, as shown in Fig. 7(a) and (b). The results for other catalysts (Ti(M)-ATA (M = Zr, Hf, Ta)) are provided in Fig. S9(a) and (b).† The indirect band gap of unmodified Ti-ATA is 1.54 eV. Compared to the unmodified Ti-ATA catalyst, the band gap of metal-modified Ti(Nb)-ATA (1.25 eV) and Ti(Ta)-ATA (1.31 eV) (VB metals in the periodic table) becomes significantly narrower and several new energy bands appear near the Fermi energy level. By contrast, the band gaps of Ti(Zr)-ATA (1.77 eV) and Ti(Hf)-ATA (1.79 eV) (IVB metals in the periodic table) are wider and there are no new energy bands near the Fermi energy level. Importantly, a new energy band consisting of transition metal d orbitals emerges near the Fermi energy level of Ti(Nb)-ATA. This energy band has an important contribution near the Fermi energy level and can be used as a doping energy level to promote the separation of photoelectrons and holes by trapping electrons, thus increasing the stability of reaction intermediates and lowering the barriers in the reduction of CO_2 to C_2H_5OH *via* photocatalysis. Charge separation is a key step in photocatalysis to convert light energy into chemical energy, and it directly impacts the performance of the catalyst. In order to further improve the activity and selectivity of CO_2 photoreduction to ethanol, we constructed bimetallic active sites by introducing a second metal component into the metal node of Ti-ATA, effectively regulated the energy band structure of the MOF material, and optimized the separation efficiency of photogenerated electrons. To further analyze the electron transfer behavior during the photocatalytic process, we further calculated the valence band maxima (VBM) and conduction band minima (CBM) of Ti-ATA and Ti(M)-ATA (M = Zr, Hf, Nb, Ta), as shown in Fig. 7(c) and S9(c).† For the unmodified Ti-ATA catalyst, the VBM is mainly located on the π-bond orbitals of the ligand, whereas the CBM is mainly located on the Ti-oxo cluster. For Ti(Nb)-ATA, electrons are transferred from the excited ATA ligand to the Nb centers, and subsequently, the Nb ions transfer electrons to Ti, forming photocatalytically active Nb ions. The calculation results suggest that the modified Ti nodes may act as electronic mediators to facilitate the transfer of electrons from the ATA ligand to the Nb site. The emergence of new energy levels in Ti(Nb)-ATA effectively inhibits the rapid electron–hole complexation and provides a more stable platform for photogenerated electrons with superior photocatalytic performance for CO_2 reduction to C_2 products. In addition, according to Bader charge analysis (Fig. S10†), the doped metal atoms transfer electrons to bridging oxygen atoms between the Ti atom and doped metal atoms, which leads to the accumulation of negative charges around the doped metal center. This result

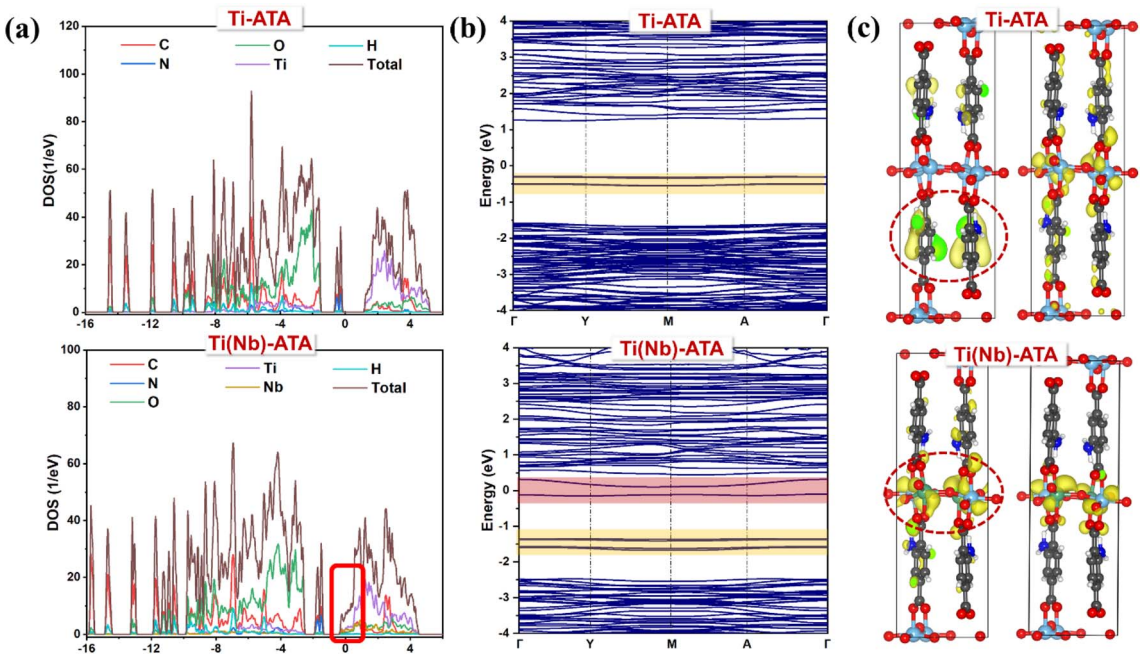

Fig. 7 The calculated (a) total and projected density of states (TDOS and PDOS), with the Fermi energy level set to zero. (b) Energy band structures of pristine Ti-ATA and metal-modified Ti(Nb)-ATA. (c) The calculated valence-band maximum (VBM) (left side) and conduction-band minimum (CBM) (right side) of pristine Ti-ATA and metal-modified Ti(Nb)-ATA.

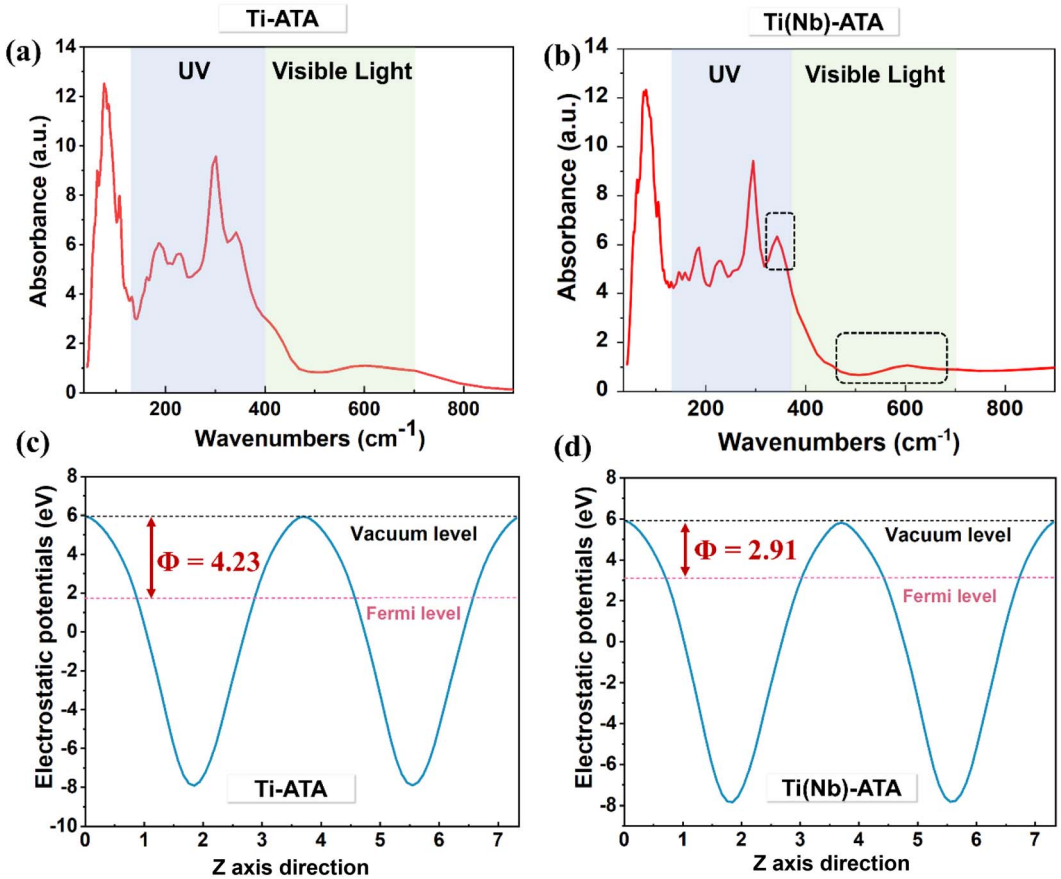

Fig. 8 The optical absorption spectra for (a) Ti-ATA and (b) Ti(Nb)-ATA. The electrostatic potential profiles of (c) Ti-ATA and (d) Ti(Nb)-ATA.

indicates that there is a significant charge transfer in the Ti–O–M (M = Zr, Hf, Nb, Ta) structure, with the Nb dopant exhibiting the greatest charge transfer, as evidenced in Fig. S10.† Thus, doping another metal into the Ti-MOF can result in a significant charge redistribution at the nodes of MOF materials. Overall, the electronic structure characteristics of pristine Ti-ATA and metal-modified Ti(M)-ATA (M = Zr, Hf, Nb, Ta) are generally consistent with the predicted activity of these candidate catalysts.

Finally, we calculated the optical absorption spectrum of Ti-ATA and Ti(Nb)-ATA, as shown in Fig. 8(a) and (b). The optical absorption of Ti-ATA and Ti(Nb)-ATA is mainly located in the ultraviolet region. However, the light absorption activity of the modified nodes was slightly improved. Due to the narrow band gap, the response of Ti(Nb)-ATA in visible and infrared bands is slightly stronger than that of Ti-ATA. The absorption spectra of other Ti(M)-ATA catalysts (M = Zr, Hf, Ta) were also calculated, as shown in Fig. S11.† In addition, the work function (Φ) is an important parameter to measure the electron gain/loss ability of materials, which is defined as the minimum energy required for electrons to escape from the interior of materials to the surface.[42,43] In DFT calculations, the work function is obtained from the electrostatic potential distribution, which is calculated using the equation $\Phi = E_V - E_f$, where E_v and E_f are the potentials of the vacuum energy level and the Fermi energy level, respectively. As shown in Fig. 8(c) and (d), the work function of Ti-ATA is calculated to be 4.23 eV (Fig. 8(c)). After the introduction of Nb atoms into the Ti node, the work function is reduced to 2.91 eV (Fig. 8(d)). The work function of other Ti(M)-ATA catalysts is also lower than that of pristine Ti-ATA (Fig. S12†). The values of the work function, vacuum energy level and Fermi energy level for Ti-ATA and Ti(M)-ATA are provided in Table S6.† Further analysis reveals that the decrease in work function is caused by an up shift in the Fermi level. As mentioned above, the electrons from the Nb atom transfer to the O atom at the node, and the Fermi level of Ti(M)-ATA is enhanced due to Nb–O bonding. The reduced work function is conducive to the transfer of electrons from Ti(M)-ATA to the surface-adsorbed species in the photocatalytic reaction, thereby improving photocatalytic activity.

4 Conclusions

In summary, by means of DFT calculations, we systematically investigated the structure and stability of a series of metal node-modified Ti(M)-ATA (Mn, Fe, Co, Ni, Cu, Zn, Zr, Nb, Mo, Ru, Rh, Pd, Hf, Ta, W, Os, Ir, Au) MOF catalysts and their applications in the photocatalytic reduction of CO_2 to C_2 chemicals. Our results show that Ti(M)-ATA (M = Zr, Hf, Nb, Ta) can sufficiently activate CO_2, and the energetically optimal pathway for the

reduction of CO_2 to C_2 products has been determined by reaction route screening. Over Ti(Nb)-ATA, Ti(Ta)-ATA, Ti(Zr)-ATA and Ti(Hf)-ATA, the two *CHO species undergo C–C coupling to form *CHOCHO, an important C_2 intermediate. Ti(Nb)-ATA and Ti(Ta)-ATA tend to generate ethanol, while Ti(Zr)-ATA and Ti(Hf)-ATA are more selective to ethylene.

Remarkably, Ti(Nb)-ATA is the best photocatalyst for C_2H_5OH production among all the candidates studied, and the corresponding optimal reduction pathway is identified as: $*CO_2 \rightarrow *OCHO \rightarrow *OCHOH \rightarrow *CHO \rightarrow *CHOCHO \rightarrow *CHOCH_2O \rightarrow *CHOHCH_2O \rightarrow *CH_2OHCH_2O \rightarrow *CH_2CH_2O + H_2O \rightarrow *CH_2CH_2OH \rightarrow *CH_3CH_2OH \rightarrow *+C_2H_5OH$, in which the hydrogenation of $*CH_2CH_2O$ species is the rate-determining step for the overall reaction with a limiting free energy change of 1.12 eV. By analyzing the correlation, it is found that the catalytic activity of these metal node-modified catalysts is highly dependent on their binding strength to the CO_2 reactant and key reaction intermediates (*e.g.* *OCHOH).

In addition, the analysis of electronic and optical properties indicates that the altered energy band structure and charge transfer characteristics at the bimetallic node of Ti(Nb)-ATA are responsible for its superior catalytic activity towards CO_2 reduction to C_2H_5OH compared to pristine Ti-ATA and other metal-modified Ti(M)-ATA candidates. The facile substitution or doping of metals in Ti-MOFs and their structural flexibility and diversity enable us to design a variety of Ti-based MOF photocatalysts with desirable properties. Our findings will stimulate further in-depth experimental studies of Ti-based MOF materials and open up new avenues for developing Ti-MOF-based catalysts for CO_2 photoreduction, especially for the synthesis of C_2 chemicals.

Data availability

The data supporting this article have been included as part of the ESI.†

Author contributions

Shuang Wang: conceptualization, methodology, data acquirement, writing – original draft preparation. Xiaowa Nie: conceptualization, supervision, methodology, data analysis, writing – review & editing. Chunshan Song: investigation, writing – review & editing. Xinwen Guo: supervision, resources, project administration, writing – review & editing.

Conflicts of interest

There are no conflicts to declare.

Acknowledgements

This work was supported by the National Natural Science Foundation of China (No. 22278056), the Fundamental Research Funds for the Central Universities (No. DUT22-LAB602), and the Liaoning Revitalization Talents Program (No. XLYC3008032). We also acknowledge the Dalian University of Technology Supercomputing Center, Tianjin Supercomputing Center, and Beijing Paratera Co., Ltd. Supercomputing Center for providing computing resources for this work.

References

1 X. Nie, W. Li, X. Jiang, X. Guo and C. Song, *Adv. Catal.*, 2019, **65**, 121–233.
2 X. Chang, T. Wang, P. Yang, G. Zhang and J. Gong, *Adv. Mater.*, 2019, **31**, 1804710.
3 W. Gao, S. Liang, R. Wang, Q. Jiang, Y. Zhang, Q. Zheng, B. Xie, C. Ying Toe, X. Zhu, J. Wang, L. Huang, Y. Gao, Z. Wang, C. Jo, Q. Wang, L. Wang, Y. Liu, B. Louis, J. Scott, A. Roger, R. Amal, H. Heh and S. Park, *Chem. Soc. Rev.*, 2020, **49**, 8584–8686.
4 N. Liu, Y. Zhao, S. Zhou and J. Zhao, *J. Mater. Chem. A*, 2020, **8**, 5688–5698.
5 H. Shi, H. Wang, Y. Zhou, J. Li, P. Zhai, X. Li, G. Gurzadyan, J. Hou, H. Yang and X. Guo, *Angew. Chem., Int. Ed.*, 2022, e202208904.
6 H. Liu, B. Sun, Z. Li, D. Xiao, Z. Wang, Y. Liu, Z. Zheng, P. Wang, Y. Dai, H. Cheng and B. Huang, *Angew. Chem., Int. Ed.*, 2024, **63**, e202410596.
7 Y. Zhao, N. Liu, S. Zhou and J. Zhao, *J. Mater. Chem. A*, 2019, **7**, 16294–16303.
8 H. Zhou, Y. Hua, Y. Zhang, W. Jiang and J. Di, *Sep. Purif. Technol.*, 2024, **16**, 1383–5866.
9 S. Ma, W. Han, W. Han, F. Dong and Z. Tang, *J. Mater. Chem. A*, 2023, **11**, 3315–3363.
10 J. Zhang, W. Yang, M. Zhang, H. Wang, R. Si, D. Zhong and T. Lu, *Nano Energy*, 2021, **80**, 105542.
11 L. Wang, S. You, Y. Gong, J. Gu, J. Zhang, G. Shan, B. Zhu, W. Yang, C. Sun, X. Wang and Z. Su, *Green Chem.*, 2024, **26**, 9415.
12 M. Zhang, D. Zhang, X. Jing, B. Xu and C. Duan, *Angew. Chem., Int. Ed.*, 2024, **63**, e202402755.
13 R. Li, W. Zhang and K. Zhou, *Adv. Mater.*, 2018, **30**, 1705512.
14 Y. Zhao, Z. Shao, Y. Cui, K. Geng, X. Meng, J. Wu and H. Hou, *Small*, 2023, **19**, 2300398.
15 X. Shi, L. Cao, M. Chen and Y. Huang, *Chin. Chem. Lett.*, 2022, **33**, 5023–5029.
16 H. Yang, G. Liu, L. Zheng, M. Zhang, Z. Guan, T. Liu and J. Yang, *Appl. Catal. B Environ.*, 2024, **359**, 124491.
17 B. Qiao, A. Wang, X. Yang, L. F. Allard, Z. Jiang, Y. Cui, J. Liu, J. Li and T. Zhang, *Nat. Chem.*, 2011, **3**, 634–641.
18 X. He, X. Gao, X. Chen, S. Hu, F. Tan, Y. Xiong, R. Long, M. Liu, E. Tse, F. Wei, H. Yang, J. Hou, C. Song and X. Guo, *Appl. Catal. B Environ.*, 2023, **327**, 122418.
19 S. Wang, X. Nie, J. Lin, F. Ding, C. Song and X. Guo, *ChemSusChem*, 2024, e202301619.
20 S. Wang, X. Nie, C. Song and X. Guo, *CCS Chem.*, 2024, **6**, 3018–3029.
21 F. Xie, C. Bie, J. Sun, Z. Zhang and B. Zhu, *J. Mater. Sci. Technol.*, 2024, **170**, 87–94.
22 J. Olowoyo, U. Saini, M. Kumar, H. Valdes, H. Singh, M. Omorogie, J. Babalola, A. Vorontsov, U. Kumar and P. Smirniotis, *J. CO2 Util.*, 2020, **42**, 101300.

23 X. Cheng, Y. Gu, X. Zhang, X. Dao, S. Wang, J. Ma, J. Zhao and W. Sun, *Appl. Catal. B Environ.*, 2021, **298**, 120524.
24 I. Tsuji, H. Kato, H. Kobayashi and A. Kudo, *J. Am. Chem. Soc.*, 2004, **126**, 13406–13413.
25 D. Sun, W. Liu, M. Qiu, Y. Zhang and Z. Li, *Chem. Commun.*, 2015, **51**, 2056–2059.
26 X. Wu, L. Gagliardi and D. Truhlar, *J. Am. Chem. Soc.*, 2018, **140**, 7904–7912.
27 M. Ming, Y. Wang, W. Tao, W. Shi, D. Zhong and T. Lu, *Green Chem.*, 2023, **25**, 6207.
28 K. Mori, J. Matsuo, Y. Kondo, H. Hata and H. Yamashita, *ACS Appl. Energy Mater.*, 2021, **4**, 11634–11642.
29 D. Lee, S. Lee, I. Choi and M. Kim, *Smart Mol.*, 2024, **2**, e20240002.
30 X. He, Y. Ding, Z. Huang, M. Liu, M. Chi, Z. Wu, C. Segre, C. Song, X. Wang and X. Guo, *Angew. Chem., Int. Ed.*, 2023, e202217439.
31 X. Cheng, X. Dao, S. Wang, J. Zhao and W. Sun, *ACS Catal.*, 2021, **11**, 650–658.
32 G. Kresse and J. Furthmüller, *Phys. Rev. B:Condens. Matter Mater. Phys.*, 1996, **54**, 11169–11186.
33 G. Kresse and J. Furthmüller, *Comp. Mater. Sci.*, 1996, **6**, 15–50.
34 S. Grimme, *J. Comput. Chem.*, 2006, **27**, 1787–1799.
35 M. Yu, S. Yang, C. Wu and N. Marom, *npj. Comput. Mater.*, 2020, **6**, 180.
36 L. Gong, D. Zhang, C. Lin, Y. Zhu, Y. Shen, J. Zhang, X. Han, L. Zhang and Z. Xia, *Adv. Energy Mater.*, 2019, **9**, 1902625.
37 S. Li, Z. Lu, Y. Zhang, D. Ma and Z. Yang, *Phys. Chem. Chem. Phys.*, 2017, **19**, 9007–9015.
38 G. Jajko, P. Gryta, P. Kozyra, M. Szufla, D. Matoga, D. Majda and W. Makowski, *J. Phys. Chem. C*, 2022, **126**, 9185–9194.
39 S. Wang, Y. Liu and J. Zhao, *Phys. Chem. Chem. Phys.*, 2020, **22**, 17639–17645.
40 Y. Sun, S. Wang, J. Jia, Y. Liu, Q. Cai and J. Zhao, *J. Mater. Chem. A*, 2022, **10**, 14460.
41 X. Gao, Z. Wang, Q. Huang, M. Jiang, S. Askari, N. Dewangan and S. Kawi, *Catal. Today*, 2022, **402**, 88–103.
42 Y. Huang, K. Dai, J. Zhang and G. Dawson, *Chin. J. Catal.*, 2022, **43**, 2539–2547.
43 B. Zhu, H. Tan, J. Fan, B. Cheng, J. Yu and W. Ho, *J. Mater.*, 2021, **7**, 988–997.